

Realization of a fractional quantum Hall state with ultracold atoms

<https://doi.org/10.1038/s41586-023-06122-4>

Received: 19 October 2022

Accepted: 24 April 2023

Published online: 21 June 2023

 Check for updates

Julian Léonard^{1,6}✉, Sooshin Kim¹, Joyce Kwan¹, Perrin Segura¹, Fabian Grusdt^{2,3}, Cécile Repellin⁴, Nathan Goldman⁵ & Markus Greiner¹

Strongly interacting topological matter¹ exhibits fundamentally new phenomena with potential applications in quantum information technology^{2,3}. Emblematic instances are fractional quantum Hall (FQH) states⁴, in which the interplay of a magnetic field and strong interactions gives rise to fractionally charged quasi-particles, long-ranged entanglement and anyonic exchange statistics. Progress in engineering synthetic magnetic fields^{5–21} has raised the hope to create these exotic states in controlled quantum systems. However, except for a recent Laughlin state of light²², preparing FQH states in engineered systems remains elusive. Here we realize a FQH state with ultracold atoms in an optical lattice. The state is a lattice version of a bosonic $v = 1/2$ Laughlin state^{4,23} with two particles on 16 sites. This minimal system already captures many hallmark features of Laughlin-type FQH states^{24–28}: we observe a suppression of two-body interactions, we find a distinctive vortex structure in the density correlations and we measure a fractional Hall conductivity of $\sigma_H/\sigma_0 = 0.6(2)$ by means of the bulk response to a magnetic perturbation. Furthermore, by tuning the magnetic field, we map out the transition point between the normal and the FQH regime through a spectroscopic investigation of the many-body gap. Our work provides a starting point for exploring highly entangled topological matter with ultracold atoms^{29–33}.

The FQH effect emerges in 2D electron gases from the combination of a magnetic field and repulsive interactions⁴. The magnetic field quenches the kinetic energy into highly degenerate Landau levels, among which the particles arrange themselves to minimize their interaction energy. In many cases, FQH states are described by Laughlin's wavefunction²³, whose characteristic pairwise correlated vortex motion results in a screening of interactions and strong anticorrelations at distances below the vortex size (Fig. 1a). FQH states show a topological robustness with exotic properties that are unseen in non-interacting systems, including quasi-particles with fractional charge, non-local topological entanglement and anyonic exchange statistics⁴.

The desire to study these phenomena in a controlled environment has triggered efforts to realize FQH states in quantum-engineered systems. Because the constituents of those platforms are typically charge-neutral, synthetic magnetic fields are introduced through the Coriolis force in rotating systems^{5–8,34} or by engineering geometric phases^{9–13,15,18,19}. Recently, interaction-induced behaviour has been observed in several systems^{14,16,20,21}, including a Laughlin state made of light²². Quantum gases in driven optical lattices³⁵ constitute a particularly promising platform to study FQH physics owing to their superb control and large attainable system sizes, yet, reaching the strongly interacting regime remains a challenge.

Here we realize a bosonic FQH state in a bottom-up approach using two particles in a driven optical lattice. The presence of few-particle

FQH states in lattice models, also called fractional Chern insulators, is numerically well established^{24–28,30,36}. Conceptually, they originate from flat Chern bands that take the role of the Landau levels. The proposed preparation schemes for those states, however, have exceeded experimental capabilities so far^{37–39}. In our work, we devise and apply a new adiabatic-state-preparation scheme, enabled by site-resolved control in a quantum gas microscope with bosonic ⁸⁷Rb (refs. 14,40) (Fig. 1b). We verify that the prepared state corresponds to the target FQH state by inverting the preparation scheme (Fig. 1c) and we sample density snapshots from the prepared state to confirm that it exhibits key properties of a FQH state, including a screening of two-body interactions, a vortex structure in the density correlations and a fractional Hall conductivity.

State preparation

The system is governed by the interacting Harper–Hofstadter model (Fig. 1c), which describes the motion of particles on a square lattice in the presence of a magnetic field. In our setup, the effective magnetic field is realized by Floquet engineering complex tunnelling amplitudes with Raman-assisted tunnelling processes³⁵ (Methods). Within the Floquet-engineered Hamiltonian, we achieve independent control of the flux $\phi/2\pi$ per unit cell, the tunnelling rates K and J along x and y , respectively, as well as the gradients Δ_x and Δ_y . The on-site interaction U remains constant and large compared with all other energy scales.

¹Department of Physics, Harvard University, Cambridge, MA, USA. ²Department of Physics and ASC, Ludwig-Maximilians-Universität München, Munich, Germany. ³Munich Center for Quantum Science and Technology (MCQST), Munich, Germany. ⁴Université Grenoble Alpes, CNRS, LPMMC, Grenoble, France. ⁵Center for Nonlinear Phenomena and Complex Systems (CENOLI), Université Libre de Bruxelles, Brussels, Belgium. ⁶Present address: Vienna Center for Quantum Science and Technology, Atominstitut, TU Wien, Vienna, Austria. ✉e-mail: julian.leonard@tuwien.ac.at

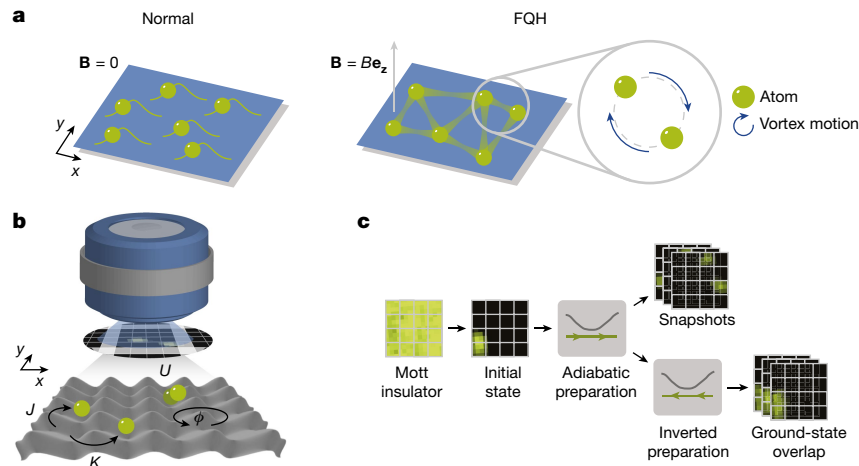


Fig. 1 | Realizing a FQH state in an optical lattice. **a**, Without a magnetic field, a 2D gas remains in a superfluid (normal) state with weak correlations. In the presence of a strong magnetic field, the system may enter a FQH state with strong correlations, which (for Laughlin states) manifest through a simultaneous vortex motion between all pairs of atoms. The system thereby minimizes interactions while incorporating the angular momentum induced by the magnetic field. **b**, We realize such a system with two bosonic ^{87}Rb atoms in an optical lattice potential with 4×4 sites. The system is placed in the focus of a high-resolution imaging system, which allows us to take projective

measurements of the quantum state with single-lattice-site resolution. The system is described by the Harper–Hofstadter model with tunnelling rates K and, along x and y , respectively, magnetic flux ϕ per plaquette and on-site interaction U . **c**, The experimental protocol begins with a Mott insulator, from which we prepare the initial state with both atoms on neighbouring edge sites. We adiabatically change the Hamiltonian parameters until reaching the FQH state. We either take snapshots of the final state or invert the preparation protocol and map the final state back to the initial state to characterize the adiabaticity of the protocol.

Our state-preparation scheme is based on an adiabatic path that keeps the finite-size gap between the ground state and the excited states open throughout the protocol. It begins from an initial state of two localized atoms in the absence of any tunnelling. First, we increase the tunnelling/along y in the presence of a gradient Δ_y , whereas tunnelling along x remains inhibited (Fig. 2a). Because J remains approximately constant for the remainder of the protocol (Methods), it sets the tunnelling time $\tau = \hbar/J = 4.3(1)$ ms and the interaction strength $U = 6.7(1)J$. Subsequently, Δ_y is adiabatically removed and we obtain a 1D system in its ground state. A similar procedure is then performed along x : tunnelling K is increased at constant flux $\phi/2\pi = 0.27$ and gradient Δ_x and then the gradient is adiabatically removed. Up to this point, we keep the tunnelling ratio at $K/J = 1.19(3)$. In a final step, we bring the tunnelling amplitudes to $K = J$ to reach the target state. At each step of the evolution, we measure the density distribution of the system and find agreement with an exact numerical prediction at the respective Hamiltonian parameters (Fig. 2b).

The asymmetric tunnelling $K > J$ is key to realizing a favourable path between the initial product state and the final FQH state. This can be understood in a coupled-wire picture⁴¹ (Methods), which interprets the single-particle spectrum as parabolic dispersions with tunnelling K , which are offset in momentum by ϕ/a . The tunnelling J creates a weak interwire coupling that enables particle motion in elongated cyclotron orbits. Repulsive interactions let particles avoid each other, resulting in a Tao–Thouless-type charge-density wave (CDW) along y . This CDW state acts as a bridge between the initial state and the final state: on the one hand, it is adiabatically connected to a 1D CDW by adding a gradient along x and, on the other hand, it is adiabatically connected to a Laughlin state with vortex binding of composite particles by ramping to isotropic cyclotron orbits at $K = J$.

The success probability of the state preparation is given by the fidelity $\mathcal{F} = \langle \psi_0 | \hat{\rho}_{\text{Final}} | \psi_0 \rangle$, which measures the overlap between the density operator $\hat{\rho}_{\text{Final}}$ describing the state after the preparation protocol and the ground state $|\psi_0\rangle$ at the final Hamiltonian parameters. Because $|\psi_0\rangle$ is a delocalized and entangled state, measuring \mathcal{F} directly with local observables is not possible. Instead, we map $|\psi_0\rangle$ back to the initial state by following the preparation with an identical but reversed protocol.

Assuming that the evolution during both ways is independent, the final ground-state population is given by \mathcal{F}^2 , which can be directly measured because it equals the probability to measure the initial density distribution. We find a dominant ground-state population throughout the evolution and a fidelity of $\mathcal{F} = 43(6)\%$ to prepare the final state (Fig. 2e).

Normal-to-FQH transition

In the thermodynamic limit, N charge carriers are expected to enter the lowest bosonic Laughlin state at a filling factor $v = N/N_\phi = 1/2$, in which N_ϕ is the number of magnetic flux quanta in the system. Including corrections for the finite size and particle number, we expect the transition in our system to occur approximately within the flux range $\phi/2\pi \approx 0.2–0.33$ (Methods). A systematic understanding of the transition point in small systems is the subject of current research²⁸. To map out the transition between the normal state and the FQH state, we use the adiabaticity of the preparation scheme as a spectroscopic signature for the energy gap (Fig. 2g). The fidelity \mathcal{F} is limited by the smallest energy gap during the preparation protocol and therefore decreases when the energy of the ground and excited states approach each other. Repeating the protocol for different flux values shows a breakdown of the adiabaticity at $\phi/2\pi \approx 0.25$, indicating the location of the transition point. The observed transition point is in agreement with exact numerical calculations of the gap diagram (Fig. 2f,g). By contrast, when repeating the measurement at $K > J$, no breakdown of adiabaticity is visible, indicating that the many-body gap remains open until we reach homogeneous tunnelling $K = J$. At low and high flux, the fidelities for $K = 1.2$ and $K = J$ coincide, indicating that the gap remains open away from the transition point. We attribute the overall downward trend of the fidelity at $K = 1.2$ to increased Floquet heating at larger flux owing to higher overlap of the drive with the first excited Bloch band⁴⁴.

Screening of interactions

A hallmark of Laughlin-type FQH states is the screening of on-site interactions resulting from the pairwise vortex motion. In our two-particle system, the interaction energy simplifies to

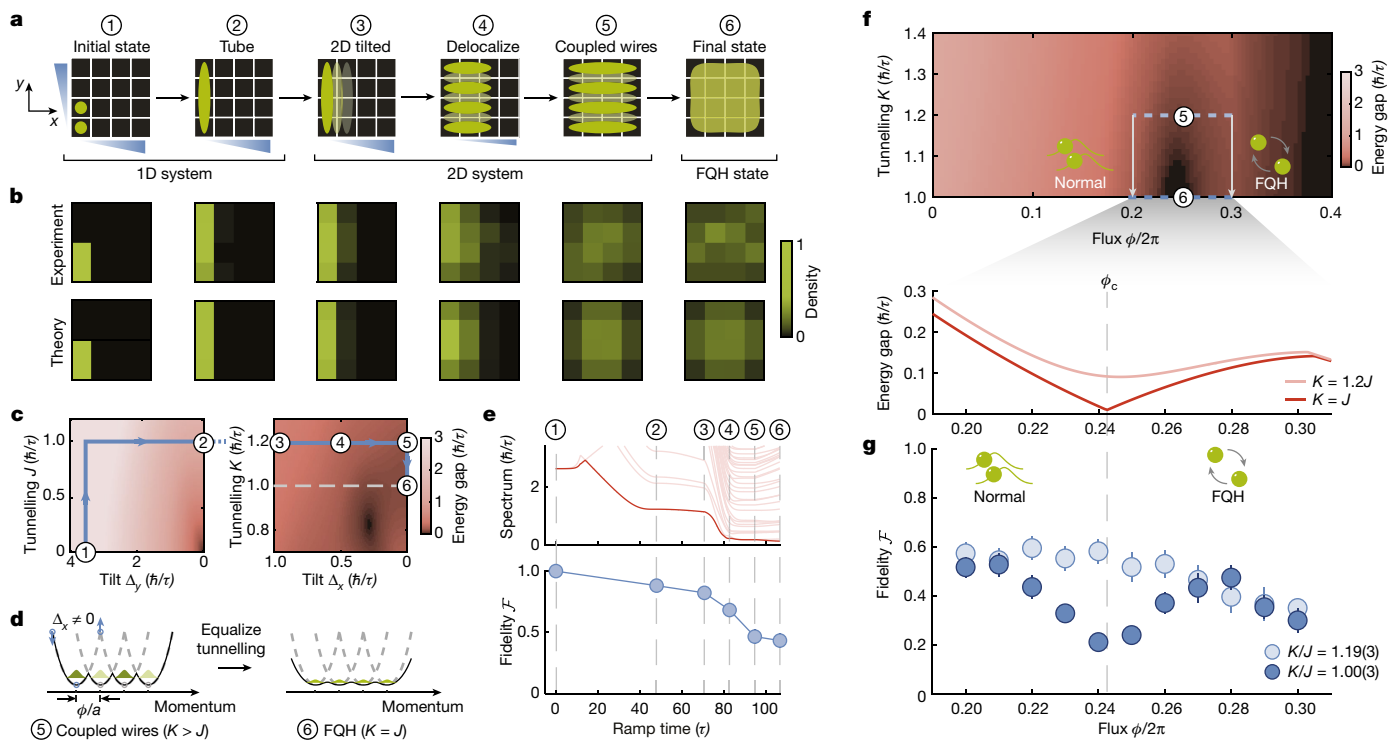


Fig. 2 | FQH state preparation and gap diagram. **a**, Adiabatic preparation.

(1) The ground state of the initial Hamiltonian corresponds to two repulsively interacting bosons on neighbouring sites. (2) Enabling tunnelling/along y and reducing the gradient Δ_y homogeneously delocalizes the particles into one column. (3) Switch on tunnelling K along x in the presence of a strong tilt and at flux $\phi/2\pi = 0.27$. (4) Particles spread over the entire 2D system as the tilt is reduced. (5) Up to this point, $K > J$, such that the system resembles coupled horizontal wires. (6) Ramp to $K = J$ to reach the final state. **b**, Measurements of the site-resolved density confirm the delocalization into the 2D box potential, in agreement with exact numerical calculations (Methods). **c**, The preparation scheme ensures optimal adiabaticity by avoiding closing of the energy gap between the ground state and the excited states (shown in units of the inverse tunnelling time $\tau = 4.3(1)$ ms), as confirmed by numerical calculations of the many-body spectrum. **d**, The robustness of the scheme can be understood in a coupled-wire picture, in which the quadratic dispersions of weakly coupled

rows are offset by multiples of the momentum ϕ/a (with a the lattice constant). Although excited single-particle states get shifted for $\Delta_x > 0$ (blue circles), the ground state in each wire remains robust. The two-body ground state is reminiscent of a CDW and adiabatically connects to a FQH state as the tunnelling ratio approaches $K = J$. **e**, We quantify the preparation fidelity through the quantum-state overlap $\mathcal{F} = \langle \psi_0 | \hat{\rho}_{\text{Final}} | \psi_0 \rangle$, inferred from measurements after inversion of the protocol. Despite a decreasing energy gap to the first (red line) and higher excited states (pink lines) in the energy spectrum during the preparation, a notable population remains in the ground state throughout the evolution. **f**, For $K = J$, the numerically calculated energy gap shows a closing, whereas it remains open for $K > J$. **g**, We spectroscopically show the gap closing through a loss of adiabaticity, signalled by a reduction of the ground-state overlap when preparing the system at the flux $\phi_c/2\pi \approx 0.25$ (dark). The reduction is absent when ending the preparation at step (5) with $K > J$ (light blue). Error bars denote the s.e.m. and are smaller than the marker size if not visible.

$E_{\text{int}} = \langle \psi_0 | \sum_i U \hat{n}_i (\hat{n}_i - 1)/2 | \psi_0 \rangle = U \times p_{\text{Doublon}}$, in which \hat{n}_i is the number operator on site i and p_{Doublon} is the global probability to observe the two particles on the same lattice site. We measure the doublon probability in two different ways. In a first set of measurements, we perform photo-association of the doublons into molecular states, whose excess energy ejects them from the lattice and converts the doublon probability p_{Doublon} into the probability to image neither atom (Fig. 3a). This process happens naturally at the beginning of the fluorescence imaging. In a second set of measurements, we break up the doublon before the imaging step and measure each of the two atoms individually (Fig. 3b; Methods). Both techniques reveal a reduction of the doublon fraction as the flux is increased beyond the transition point. Our results agree with exact numerical calculations for the ground state. When approximately accounting for the imperfect preparation fidelity by assuming only half the population to be in the ground state, we numerically find a reduced contrast of the doublon suppression.

Correlated vortex motion

The mechanism from which the screening of interactions originates is the pairwise correlated vortex motion. In a simplified picture, the $v = 1/2$ Laughlin state can be thought of as a correlated motion in which each

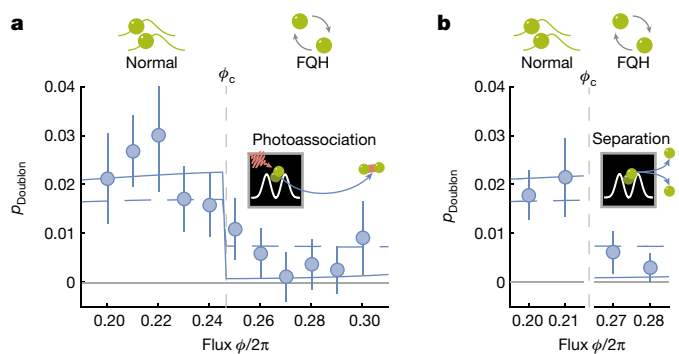


Fig. 3 | Suppression of two-body interactions. We find a reduction of the doublon fraction in the FQH state, showing the screening of interactions in the many-body wavefunction. **a**, Doublon-fraction measurement by photoassociation, converting the doubly occupied lattice site into an empty one. **b**, Doublon-fraction measurement by separating the particles on two different lattice sites before fluorescence imaging. Solid lines show exact calculations for the ground state and dashed lines take into account the finite ground-state overlap (Methods). All error bars denote the s.e.m.

particle remains bound to the core of a doubly charged vortex around every other particle. This results in a flat overall bulk density; however, the density correlations contain information about the underlying vortex structure. Averaging over many independent experimental realizations, we determine the reduced density correlations

$$g^{(2)}(\mathbf{d}) = \frac{N}{N-1} \frac{1}{N_{\text{Bulk}}} \sum_{\mathbf{i}, \mathbf{i}+\mathbf{d}} \frac{\langle \hat{a}_{\mathbf{i}}^\dagger \hat{a}_{\mathbf{i}+\mathbf{d}}^\dagger \hat{a}_{\mathbf{i}+\mathbf{d}} \hat{a}_{\mathbf{i}} \rangle}{\langle \hat{a}_{\mathbf{i}}^\dagger \hat{a}_{\mathbf{i}} \rangle \langle \hat{a}_{\mathbf{i}+\mathbf{d}}^\dagger \hat{a}_{\mathbf{i}+\mathbf{d}} \rangle}, \quad (1)$$

in which the creation (annihilation) of a boson on site \mathbf{i} is described by the operator $\hat{a}_{\mathbf{i}}^\dagger (\hat{a}_{\mathbf{i}})$. We average over all terms with \mathbf{i} and/or $\mathbf{i} + \mathbf{d}$ within the $N_{\text{Bulk}} = 4$ central bulk sites to obtain the reduced correlations at relative particle distance vector $\mathbf{d} = (d_x, d_y)$. The prefactor normalizes the correlations for finite particle number N such that $g^{(2)}(\mathbf{d})$ is larger (smaller) than unity if the densities are correlated (anticorrelated). By construction, the correlator is inversion-symmetric, that is, $g^{(2)}(\mathbf{d}) = g^{(2)}(-\mathbf{d})$. In the normal regime, we observe approximately homogeneous correlations, whereas the FQH regime shows a contrast in correlations with increasing distance (Fig. 4a). To quantitatively analyse the density correlations, we compute the azimuthal average as a function of distance $|\mathbf{d}|$. Although the normal state remains mostly uncorrelated, the FQH state shows anticorrelations up to $r \lesssim \sqrt{2}$ sites and increased correlations for $r \gtrsim 2$ sites (Fig. 4b). Taking into account that the core size of a doubly charged vortex is about twice the magnetic length $l_B = 1/\sqrt{\phi} \approx 0.8$ sites, the observed pair correlations are consistent with the pattern of particles binding to doubly charged vortices. When measuring the correlations for different flux, we find that the onset of the vortex pattern coincides with the previously established transition point of $\phi/2\pi \approx 0.25$ (Fig. 4c).

Fractional Hall conductivity

Our observed FQH properties suggest that, despite its small size, our system may already exhibit precursors of a topological robustness. The paradigmatic signature of FQH states is the Hall conductivity $\sigma_H = C\sigma_0$, which, normalized by the von Klitzing constant $\sigma_0^{-1} = R_K$, is directly related to the topological many-body Chern number C . Although the Hall conductivity is a transport property, it is also encoded into the density distribution of the system through Středa's formula^{28,42–44}:

$$\frac{\partial \rho_{\text{Bulk}}}{\partial (\phi/2\pi)} = \frac{\sigma_H}{\sigma_0} \equiv C. \quad (2)$$

Středa's formula predicts an increase in the bulk density as a response to an increasing magnetic field that is directly proportional to the Hall conductivity. In an isolated system (such as ours), the response of the bulk density is enabled by particle exchange with the edge. Founded on general thermodynamics relations, it is valid for any insulating state⁴, including strongly correlated states, and has been explicitly verified for few-particle FQH states on a lattice²⁸. We measure the response of the density to an increasing flux and observe an enhanced bulk density within the FQH regime (Fig. 5a). We investigate the particle density on all bulk sites and find a linear increase, from which we derive the Hall conductivity $\sigma_H/\sigma_0 = 0.6(2)$ through a linear fit to the data. The non-zero Hall conductivity implies that the prepared state is chiral. Furthermore, the obtained value is consistent with the exact numerical prediction of $\sigma_H/\sigma_0 = 0.6$ for the ground state and it is comparable with the expected value of $\sigma_H/\sigma_0 = 1/2$ for the $v = 1/2$ FQH state in the thermodynamic limit. These findings signal the precursor of a topological (quantized) response in the system. We find numerically that populations in the lowest excited states decrease the bulk density; however, for moderate variations in the ground-state fidelity (as measured in Fig. 2g), the resulting change of the Hall conductivity is smaller than the uncertainty from the fit.

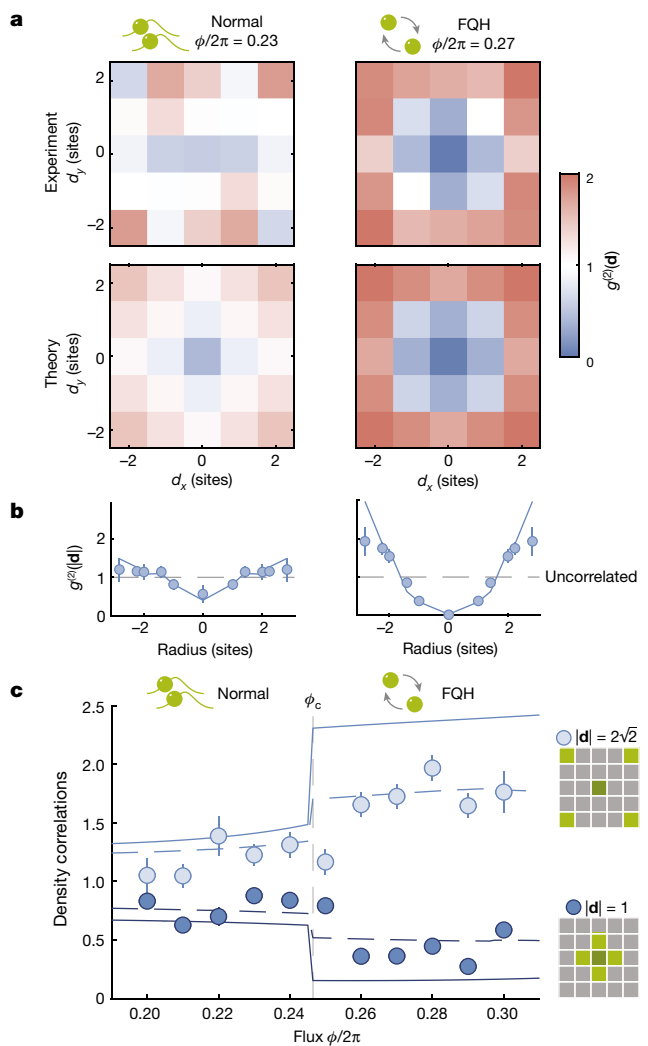


Fig. 4 | Vortex structure of correlations. **a**, The density correlations (averaged over all bulk sites) $g^{(2)}(\mathbf{d})$ show a homogeneous behaviour in the normal regime, whereas they show a ring structure in the FQH regime. By construction, the correlations are inversion-symmetric. **b**, The radial average shows how correlations in the FQH state are suppressed at short distance and enhanced at larger distance compared with the trivial state, in agreement with binding to a doubly charged vortex. **c**, The divergence between correlations at short distance ($|\mathbf{d}| = 1$) and large distance ($|\mathbf{d}| = 2\sqrt{2}$) coincides with the previously established transition point. Solid lines show exact calculations for the ground state and dashed lines take into account the finite ground-state overlap (Methods). Error bars denote the s.e.m.

Discussion and outlook

Our work establishes ultracold atoms as a viable platform to study strongly correlated topological matter. The results provide a basis for extensions in several directions. Extracting the many-body Chern number from Hall responses^{28,45} or randomized measurements⁴⁶ is within reach for comparable system sizes. Realizing larger systems is challenging owing to their reduced finite-size gap, which requires enhanced coherence times to maintain a substantial ground-state overlap during the adiabatic preparation. Several approaches are being explored at present to improve the coherence of Floquet systems, for instance, by destructive interference of heating channels⁴⁷. Those larger systems host more complex FQH states such as Pfaffian states with non-Abelian anyonic excitations^{30,33}. Furthermore, methods to isolate and move fractional quasi-particles with local potentials³¹ and impurities^{29,32} can be implemented in our system, paving the way

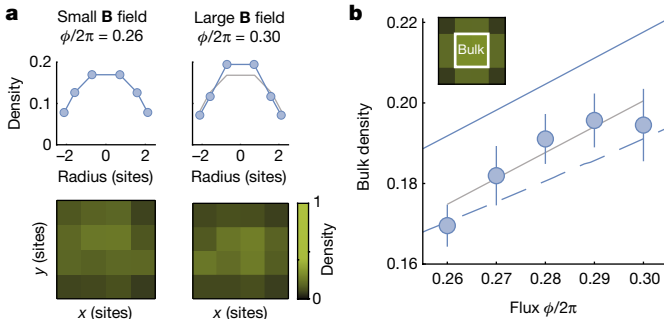


Fig. 5 | Fractional Hall conductivity. **a**, Radial averages of the density (always for total particle number $N=2$) show an enhanced probability to occupy the bulk sites for larger flux, in agreement with Středa's prediction. The grey line in the right subplot repeats the experimental data from the left panel for comparison. **b**, The bulk density is related to the Hall conductivity through the derivative $\partial\rho_{\text{bulk}}/\partial(\phi/2\pi) = \sigma_h/\sigma_0$, in which $\sigma_0^{-1} = R_K$ is the von Klitzing constant. We extract a Hall conductivity $\sigma_h/\sigma_0 = 0.6(2)$ through a linear fit (grey line) to the data, in agreement with the fractional value $\sigma_h/\sigma_0 = 1/2$ in the thermodynamic limit. The solid blue line shows exact calculations for the ground state and the dashed blue line takes into account the finite ground-state overlap (Methods). Error bars denote the s.e.m.

towards experiments on braiding statistics and fault-tolerant quantum information processing.

Online content

Any methods, additional references, Nature Portfolio reporting summaries, source data, extended data, supplementary information, acknowledgements, peer review information; details of author contributions and competing interests; and statements of data and code availability are available at <https://doi.org/10.1038/s41586-023-06122-4>.

- Wen, X. G. *Quantum Field Theory of Many-Body Systems* (Oxford Univ. Press, 2007).
- Kitaev, A. Y. Fault-tolerant quantum computation by anyons. *Ann. Phys.* **303**, 2–30 (2002).
- Nayak, C., Simon, S. H., Stern, A., Freedman, M. & Das Sarma, S. Non-Abelian anyons and topological quantum computation. *Rev. Mod. Phys.* **80**, 1083–1159 (2008).
- Giuliani, G. & Vignale, G. *Quantum Theory of the Electron Liquid* (Cambridge Univ. Press, 2012).
- Madison, K. W., Chevy, F., Wohlleben, W. & Dalibard, J. Vortex formation in a stirred Bose-Einstein condensate. *Phys. Rev. Lett.* **84**, 806 (2000).
- Schweikhard, V., Coddington, I., Engels, P., Mogendorff, V. & Cornell, E. Rapidly rotating Bose-Einstein condensates in and near the lowest Landau level. *Phys. Rev. Lett.* **92**, 040404 (2004).
- Zwierlein, M. W., Abo-Shaeer, J. R., Schirotzek, A., Schunck, C. H. & Ketterle, W. Vortices and superfluidity in a strongly interacting Fermi gas. *Nature* **435**, 1047–1051 (2005).
- Cooper, N. R. Rapidly rotating atomic gases. *Adv. Phys.* **57**, 539–616 (2008).
- Lin, Y.-J., Compton, R. L., Jiménez-García, K., Porto, J. V. & Spielman, I. B. Synthetic magnetic fields for ultracold neutral atoms. *Nature* **462**, 628–32 (2009).
- Jotzu, G. et al. Experimental realization of the topological Haldane model with ultracold fermions. *Nature* **515**, 237–240 (2014).
- Aidelsburger, M. et al. Measuring the Chern number of Hofstadter bands with ultracold bosonic atoms. *Nat. Phys.* **11**, 162–166 (2015).
- Mancini, M. et al. Observation of chiral edge states with neutral fermions in synthetic Hall ribbons. *Science* **349**, 1510–1513 (2015).
- Kennedy, C. J., Burton, W. C., Chung, W. C. & Ketterle, W. Observation of Bose-Einstein condensation in a strong synthetic magnetic field. *Nat. Phys.* **11**, 859–864 (2015).
- Tai, M. E. et al. Microscopy of the interacting Harper-Hofstadter model in the two-body limit. *Nature* **546**, 519–523 (2017).
- An, F. A., Meier, E. J. & Gadway, B. Direct observation of chiral currents and magnetic reflection in atomic flux lattices. *Sci. Adv.* **3**, e1602685 (2017).
- Roushan, P. et al. Chiral ground-state currents of interacting photons in a synthetic magnetic field. *Nat. Phys.* **13**, 146–151 (2017).

- Cooper, N. R., Dalibard, J. & Spielman, I. B. Topological bands for ultracold atoms. *Rev. Mod. Phys.* **91**, 15005 (2019).
- Asteria, L. et al. Measuring quantized circular dichroism in ultracold topological matter. *Nat. Phys.* **15**, 449–454 (2019).
- Ozawa, T. et al. Topological photonics. *Rev. Mod. Phys.* **91**, 15006 (2019).
- Mukherjee, B. et al. Crystallization of bosonic quantum Hall states in a rotating quantum gas. *Nature* **601**, 58–62 (2022).
- Zhou, T.-W. et al. Observation of universal Hall response in strongly interacting fermions. Preprint at <http://arxiv.org/abs/2205.13567> (2022).
- Clark, L. W., Schine, N., Baum, C., Jia, N. & Simon, J. Observation of Laughlin states made of light. *Nature* **582**, 41–45 (2020).
- Laughlin, R. B. Anomalous quantum Hall effect: an incompressible quantum fluid with fractionally charged excitations. *Phys. Rev. Lett.* **50**, 1395–1398 (1983).
- Hafezi, M., Sørensen, A. S., Demler, E. & Lukin, M. D. Fractional quantum Hall effect in optical lattices. *Phys. Rev. A* **76**, 023613 (2007).
- Palmer, R. N., Klein, A. & Jaksch, D. Optical lattice quantum Hall effect. *Phys. Rev. A* **78**, 013609 (2008).
- Möller, G. & Cooper, N. R. Composite fermion theory for bosonic quantum Hall states on lattices. *Phys. Rev. Lett.* **103**, 105303 (2009).
- Scaffidi, T. & Möller, G. Adiabatic continuation of fractional Chern insulators to fractional quantum Hall states. *Phys. Rev. Lett.* **109**, 246805 (2012).
- Repelin, C., Léonard, J. & Goldman, N. Fractional Chern insulators of few bosons in a box: Hall plateaus from center-of-mass drifts and density profiles. *Phys. Rev. A* **102**, 063316 (2020).
- Grusdt, F., Yao, N. Y., Abanin, D., Fleischhauer, M. & Demler, E. Interferometric measurements of many-body topological invariants using mobile impurities. *Nat. Commun.* **7**, 11994 (2016).
- Sterdyniak, A., Regnault, N. & Möller, G. Particle entanglement spectra for quantum Hall states on lattices. *Phys. Rev. B* **86**, 165314 (2012).
- Računas, M., Ünal, F. N., Anisimovas, E. & Eckardt, A. Creating, probing, and manipulating fractionally charged excitations of fractional Chern insulators in optical lattices. *Phys. Rev. A* **98**, 063621 (2018).
- Muñoz de las Heras, A., Macaluso, E. & Carusotto, I. Anyonic molecules in atomic fractional quantum Hall liquids: a quantitative probe of fractional charge and anyonic statistics. *Phys. Rev. X* **10**, 41058 (2020).
- Palm, F. A. et al. Bosonic Pfaffian state in the Hofstadter-Bose-Hubbard model. *Phys. Rev. B* **103**, L161101 (2021).
- Gemelke, N., Sarajlic, E. & Chu, S. Rotating few-body atomic systems in the fractional quantum Hall regime. Preprint at <https://arxiv.org/abs/1007.2677> (2010).
- Eckardt, A. Colloquium: Atomic quantum gases in periodically driven optical lattices. *Rev. Mod. Phys.* **89**, 011004 (2017).
- Palm, L., Grusdt, F. & Preiss, P. M. Skyrmion ground states of rapidly rotating few-fermion systems. *New J. Phys.* **22**, 083037 (2020).
- Barkeshli, M., Yao, N. Y. & Laumann, C. R. Continuous preparation of a fractional Chern insulator. *Phys. Rev. Lett.* **115**, 026802 (2015).
- Motruk, J. & Pollmann, F. Phase transitions and adiabatic preparation of a fractional Chern insulator in a boson cold-atom model. *Phys. Rev. B* **96**, 165107 (2017).
- He, Y. C., Grusdt, F., Kaufman, A., Greiner, M. & Vishwanath, A. Realizing and adiabatically preparing bosonic integer and fractional quantum Hall states in optical lattices. *Phys. Rev. B* **96**, 201103(R) (2017).
- Bakr, W. S., Gillen, J. I., Peng, A., Fölling, S. & Greiner, M. A quantum gas microscope for detecting single atoms in a Hubbard-regime optical lattice. *Nature* **462**, 74–77 (2009).
- Kane, C. L., Mukhopadhyay, R. & Lubensky, T. C. Fractional quantum Hall effect in an array of quantum wires. *Phys. Rev. Lett.* **88**, 036401 (2002).
- Widom, A. Thermodynamic derivation of the Hall effect current. *Phys. Lett.* **90**, 474 (1982).
- Středa, P. Quantised Hall effect in a two-dimensional periodic potential. *J. Phys. C Solid State Phys.* **15**, L717–L721 (1982).
- Umucalilar, R. O., Zhai, H. & Oktel, M. Ö. Trapped Fermi gases in rotating optical lattices: realization and detection of the topological Hofstadter insulator. *Phys. Rev. Lett.* **100**, 070402 (2008).
- Repelin, C. & Goldman, N. Detecting fractional Chern insulators through circular dichroism. *Phys. Rev. Lett.* **122**, 166801 (2019).
- Cian, Z. P. et al. Many-body Chern number from statistical correlations of randomized measurements. *Phys. Rev. Lett.* **126**, 50501 (2021).
- Viebahn, K. et al. Suppressing dissipation in a Floquet-Hubbard system. *Phys. Rev. X* **11**, 11057 (2021).

Publisher's note Springer Nature remains neutral with regard to jurisdictional claims in published maps and institutional affiliations.

Springer Nature or its licensor (e.g. a society or other partner) holds exclusive rights to this article under a publishing agreement with the author(s) or other rightsholder(s); author self-archiving of the accepted manuscript version of this article is solely governed by the terms of such publishing agreement and applicable law.

© The Author(s), under exclusive licence to Springer Nature Limited 2023

Article

Methods

Experimental details

Mott insulator. In each experimental realization, we prepare a Bose–Einstein condensate of bosonic ^{87}Rb atoms in the $|F=1, m_F=-1\rangle$ hyperfine state, which is loaded into a single plane of a 1D lattice along the z direction with $a_z = 1.5 \mu\text{m}$ lattice constant and $250 E_{\text{R}}$, in which $E_{\text{R}} = \hbar^2/(2ma_z^2) = \hbar \times 0.25 \text{ kHz}$ is the recoil energy for an ^{87}Rb atom of mass m . This lattice will stay on for the remainder of the experiment. We generate a superfluid with well-defined particle number from this quantum gas by first isolating a controlled number of atoms from the gas with an attractive dimple beam and then loading them into a ring-shaped repulsive potential. The Mott insulating state is then reached by ramping up two optical lattices along x and y with lattice constants $a = 680 \text{ nm}$ and depths $V_x = V_y = 45 E_{\text{R}}$ over 250 ms to create a repulsive 2D square lattice, in which $E_{\text{R}} = \hbar \times 1.24 \text{ kHz}$ is the recoil energy.

Initial-state preparation. The initial two-atom state is prepared from the Mott insulator by holographically shaping two laser beams at 760 nm with digital micro-mirror devices (DMDs, model DLP5500 from Texas Instruments) to project site-resolved, repulsive potentials onto the optical lattice. The DMDs are placed in the Fourier plane with respect to the atoms, which allows us to project diffraction-limited arbitrary potentials that correct for optical wavefront aberrations in the imaging system⁴⁸. The procedure is similar to that described in ref. 49. In brief, we first optically confine a single line of lattice sites along y within the unity-filling shell of the Mott insulator and subsequently reduce down V_x . All atoms outside the confinement potential are ejected with a repulsive deconfinement beam of large Gaussian shape, whereas the atoms within the projected confinement potential remain pinned on their lattice site. We then increase the lattice depth back to $V_x = 45 E_{\text{R}}$ and remove the confining DMD potential. In a second step, we select two atoms out of the single line of atoms by projecting a TEM20-like potential along y and subsequently reducing down V_y . After removing all atoms outside the projected potential with the deconfinement beam, we end up with the initial two-atom state with a success rate of typically 95%. After post-selecting for the atom number $N = 2$, this procedure results in an initial state fidelity of 99.1(2)%.

Floquet engineering. The Harper–Hofstadter Hamiltonian is generated through Floquet driving in the Bose–Hubbard model. The setup is described in detail in previous work¹⁴. In brief, we send two laser beams at a wavelength of 760 nm through the high-resolution objective, which overlap at the position of the atoms. The two beams have a detuning of $\omega_{\text{Raman}} = 2\pi \times 700 \text{ Hz}$ with each other and therefore generate a moving lattice in the imaging plane. The angle of incidence of the beams can be controlled with piezo mirrors that are positioned in a plane that is conjugate to the atomic plane. We choose the angle such that the interference pattern has a wavevector of $k_x = \pi/a$ along x , that is, with twice the lattice constant. The angle along y determines the Peierls phase ϕ per plaquette by $k_y = \phi/a$. The moving lattice also creates an off-resonant Floquet drive along the non-tilted direction, which leads to a renormalization of J by the factor $j_0(V_{\text{Raman}}/\hbar\omega_{\text{Raman}}) \approx 0.9$ in the final state. This is taken into account for the ratios K/J given in the manuscript. At the end of the preparation protocol, the interaction strength in units of J is therefore $U = 8.1(1)J$. To simplify the description of Fig. 2, we show all parameters in units of the bare tunnelling time τ . We also restrict the discussion to the effective Hamiltonian. A detailed representation of the preparation scheme in terms of the driven Bose–Hubbard model is shown in Extended Data Fig. 1.

Fluorescence imaging and photoassociation. The fluorescence imaging is performed after handing over the atoms to a lattice at 795 nm with the same lattice constant $a = 680 \text{ nm}$ as the previous lattice.

Doublon splitting. For the data in Figs. 2e,g and 3b, we use a full-counting procedure to split the doublon before fluorescence imaging, similar to that described in ref. 49. In brief, we first capture the atoms in a deep optical lattice. We then abruptly lower V_x such that the atoms can expand freely within each row while we switch on a vertical wall potential between the first and second columns of the system. After a short evolution time, we recapture the atoms on either side of the wall. Each atom distribution corresponds to a different Fock state. The populations of states involving atoms in the right side of the system are not resolved individually but only their sum. For Fig. 3b, we remove atoms from the right half of the system before the expansion. In this case, double occupancies of left (right) half-rows signal the presence of a doublon on the left edge (left bulk) lattice site in the respective row.

Calibration. The tunnelling amplitudes J and K are calibrated by fitting the density after a single-particle quantum walk with $n(i, t) = j_i(Kt)$, in which j_i are the Bessel functions of the first kind and i is the distance from the initial site. The interaction strength is calibrated through amplitude modulation of the lattice in the presence of a tilt. We also use amplitude modulation to calibrate the potential gradients Δ_x and Δ_y . The flux is calibrated with a precision of $\Delta\phi/2\pi = \pm 0.013$ by imaging the interference pattern of the Raman beams on a camera and extracting its wavevector through a fit.

Coherence time. We perform Bloch oscillations of a single atom starting on one lattice site to measure the coherence time in the presence of Raman driving (Extended Data Fig. 2). We find a 1/e lifetime of $\tau_{\text{Raman}} = 1.25(7) \text{ s}$.

Box potential shaping. We use the first DMD to project two wall potentials along y to confine the system along the x direction. Each wall has a Gaussian shape along x with a $1/e^2$ width of $w_0 = 0.7$ sites and is positioned at a distance of 1.5 lattice sites away from the edge site. Along y , the wall has a smoothed flat-top profile with an extension of about 10 lattice sites. We choose a wall height of 3.3 kHz such that the energy offset on the first site outside the system is larger than the Raman frequency to suppress possible resonances. The Gaussian distribution of the wall potential also causes a small energy offset on the edge site, which we confirm through density measurements in the static Bose–Hubbard system to be $< 6(1) \text{ Hz}$, small compared with the tunnelling. With the second DMD, we generate two wall potentials of the same kind along x to confine the system along the y direction.

Data analysis

Density. We obtain the mean density on each site by averaging the site occupations from the density snapshots. This procedure neglects contributions from doublons; however, this effect is small compared with our statistical error.

Fidelity measurements. We compute the ground-state fidelity as the fraction of snapshots showing the initial density distribution after inverting the preparation scheme. This protocol also maps all excited states back to different initial density distributions, which allows us to determine their populations. We confirm that all excited-state populations remain small compared with the ground-state population. See section titled ‘Excited-state populations’ for more details.

Doublon measurement. For the photoassociation measurement, the doublon fraction is given by $p_{\text{Doublon}} = p_0 - p_{\text{Offset}}$, in which p_0 is the probability to detect zero atoms. The offset probability p_{Offset} contains errors in state preparation (zero atoms in the initial state), during the evolution (loss of both particles during the preparation) and the detection fidelity (false negative to detect zero particles instead of two). We calibrate the last of these through repeated measurements of a Mott insulating state.

The first two contributions are calibrated by fluorescence imaging of the final state after a short expansion in the lattice, which separates the two atoms. For the separation measurement, we detect the doublons with a full-counting procedure described in earlier work¹⁴. Because the procedure only works for two columns, we first remove the particles in one half of the system and then detect the doublons in the remaining half. The total doublon fraction shown in Fig. 3b is twice the detected doublon fraction.

Density correlations. To extract the correlation function $g^{(2)}(\mathbf{i}, \mathbf{j})$, we first compute the correlation for each pair of sites (\mathbf{i}, \mathbf{j}) within each snapshot and then average them over all snapshots. We then move to the relative coordinate $\mathbf{d} = \mathbf{i} - \mathbf{j}$ by keeping the position of particle \mathbf{i} fixed and averaging over all available sites \mathbf{j} . We only take into account correlations with at least one particle on one of the four bulk sites. To obtain the radial average $g^{(2)}(|\mathbf{d}|)$, we compute the mean of the correlations over all pairs of sites with the same Euclidean distance $|\mathbf{d}|$. Our density snapshots do not account for on-site correlations because these are determined by the doublon probability. The on-site correlations are given by $g^{(2)}(\mathbf{d} = 0) = (\sum_{i \in \text{Bulk}} p_{\text{Doublon}, i} / \langle \hat{n}_i^2 \rangle) / N_{\text{Bulk}} \times N / (N - 1)$, in which $p_{\text{Doublon}, i}$ is the probability for a doublon on site i . We use the doublon measurements from Fig. 3b at flux $\phi/2\pi = 0.21$ ($\phi/2\pi = 0.27$) to extract $p(\hat{n}_i = 2)$ in the normal (FQH) regime. The resulting on-site correlations are those shown in Fig. 4a,b.

Fractional Hall conductivity. We obtain the mean density on each site as described above. We then compute the bulk density by taking the mean over the densities on the four central sites. For the linear fit, we only include data for $\phi/2\pi \geq 0.26$ to remove contributions from adiabaticity breakdown at the transition point.

Uncertainties. All given uncertainties are s.e.m. and are computed through bootstrapping.

Excited-state populations

In the same way that the ground-state overlap $\mathcal{F} = p_0 = \langle \psi_0 | \hat{\rho}_{\text{Final}} | \psi_0 \rangle$ is determined by the probability to recover the initial density distribution after reversing the preparation protocol, the overlaps $p_i = \langle \psi_i | \hat{\rho}_{\text{Final}} | \psi_i \rangle$ with excited states $i \geq 2$ appear as density distributions different from the initial state. The histogram of density patterns therefore provides information about the population of the individual excited states. Assuming that $p_i \ll p_0$ and neglecting transfer between excited states during the reversed preparation, the adiabatic transfer during the preparation and the reversion is the same and the final population of state i is given by $2p_i$.

With our full-counting protocol, we are able to detect the atom number on each site in the left column, as well as the sum of the atom numbers in each row of the other three columns (Extended Data Fig. 3a). Sorted by energy, eigenstates 1–10 after inversion involve both atoms in the left column, eigenstates 11–36 involve both atoms in the left two columns and all higher eigenstates up to the Hilbert space dimension 136 involve at least one atom in the right two columns of the system. As a consequence, the protocol allows us to determine all excited-state populations individually if only eigenstates 1–36 are occupied; populations in higher eigenstates are measured together with the respective eigenstate with both atoms in the left two columns.

The inferred populations are shown in Extended Data Fig. 3b for flux $\phi/2\pi = 0.27$. We find all excited-state populations to be small compared with the population of the ground state.

Numerical simulation

All theoretical predictions were obtained by exact diagonalization of the interacting Harper–Hofstadter Hamiltonian for $U = 8J$. The results in Fig. 2 were obtained by computing the energy difference between the lowest two eigenvalues. The ground-state predictions for Figs. 3–5 were

computed from the lowest eigenstate. We also compute a numerical prediction for a mixed state to have a closer comparison with the prepared state. The dashed lines in Figs. 3–5 show the results for a statistical average of 50% of the ground-state population, in which the remaining population was randomly distributed over the lowest ten excited states.

Adiabatic preparation scheme

The adiabatic preparation scheme introduced in the main text realizes a favourable path connecting the initial product state to the two-particle lattice Laughlin state. As we now discuss, interactions, gradients and kinetic terms complement each other along the chosen route and lead to minimal frustration, which ultimately leads to the large finite-size gap observed along the entire path.

In the first step, the initial two-site Mott state is melted into a 1D liquid. The large on-site interactions effectively fermionize the bosons in this step, allowing to balance kinetic and interaction energies by introducing Pauli-type correlations. In the small four-site system with hard walls, this fermionized state has a strong CDW character. In the second step, this CDW-like state is adiabatically stretched along the x direction by lowering the gradient in this direction. Because the tunnelling along x exceeds the tunnelling along y , and the synthetic magnetic field is switched on, the particles remain localized in single-particle states resembling elongated cyclotron orbits. This allows them to minimize their kinetic (single-particle) energy while maintaining a strong CDW character that simultaneously minimizes interaction energies. The state reached at the end of this step resembles a Tao–Thouless CDW along y , which is known to be adiabatically connected to the isotropic Laughlin-like state. The latter is reached in the last step by equalizing hopping amplitudes along x and y , which renders the underlying cyclotron orbits spatially isotropic. This still minimizes the kinetic and interaction energies without causing frustration: now vortex binding fermionizes the underlying bosons and a liquid of composite fermions is realized, that is, the two-particle Laughlin state.

Shape of the adiabatic ramp

All lattice and DMD laser beam powers are ramped exponentially in time. The tilt lowering along y is performed with a local adiabatic ramp, which optimizes the total adiabaticity for a given ramp duration by adapting the speed to the instantaneous many-body gap. We define the adiabaticity parameter γ through the differential equation:

$$1/\gamma = \frac{\partial \Delta_y(t)/\partial t}{\delta^2(\Delta_y)}. \quad (3)$$

Here $\delta(\Delta_y) = E_1(\Delta_y) - E_0(\Delta_y)$ is the instantaneous gap between the ground state and the first excited state and $\Delta_y(t)$ is the profile of the tilt along y during the ramp. The local adiabatic ramp follows the specific profile $\Delta_y(t)$ that solves the above differential equation for a fixed y . The ramp is adiabatic in the limit $\gamma \gg 1$. Here we use a generalized form of the above differential equation that takes into account the lowest ten excited states and also weighs them by the overlap matrix element with the ground state.

We use a local adiabatic ramp computed in the same way when decreasing Δ_x . During the last step of the preparation scheme (decreasing K from $K > J$ to $K = J$), the many-body gap remains almost constant, hence the local adiabatic ramp becomes approximately linear. We therefore use a linear ramp during this step.

On the existence of few-boson FQH states

In the following, we discuss several aspects concerning the existence of FQH states in interacting Harper–Hofstadter systems with few bosons. First, we verify that the experimentally observed signatures are genuine FQH properties and not related to the discreteness of the lattice potential. We then use further, numerically accessible observables to identify the FQH state: the orbital occupations and (through

Article

comparison with an $N = 4$ system) topological quasi-hole excitations in the particle-entanglement spectrum (PES). Finally, we close with a qualitative discussion on the circumstances at which further FQH states than the $v = 1/2$ state may exist in few-boson systems.

Lattice-continuum crossover. We numerically verify that the observed signatures are genuine properties of the $v = 1/2$ FQH state and we hereby discuss their robustness to finite-size effects. This is done by exploring the lattice-continuum crossover with a system-size scaling at constant particle number $N = 2$. Consequently, the flux per plaquette at which the FQH state appears decreases $\phi_c/2\pi \rightarrow 0$ as the system size is increased. In Extended Data Fig. 4, we show exact diagonalization calculations for the experimental signatures for system sizes ranging from 3×3 sites to 14×14 sites, whereas the particle number remains constant at $N = 2$. We find that already the 3×3 system qualitatively agrees with the FQH state for all signatures:

Gap diagram (Fig. 2): in the left panel of Extended Data Fig. 4a, we show the energy gap between the ground state and the first excited state as a function of the flux $\phi/2\pi$. We find a single gap closing around $\phi_c/2\pi \approx 0.32$, marking the transition point between the normal and FQH states. For imbalanced tunnelling $K > J$, the gap closing disappears. The gap diagram looks qualitatively similar for all considered system sizes $L \times L$.

As L increases, we find that the flux $\phi_c/2\pi$ at which the gap closing occurs becomes reduced. We extract the filling using $v_c = \rho_{\text{Bulk}}/(\phi_c/2\pi)$, in which ρ_{Bulk} is the density in the bulk region, averaged over all sites within a radius of $3l_B = 3/\sqrt{\phi}$ sites from the centre of the system. Our choice of the bulk extension ensures a sufficiently large number of lattice sites to obtain a stable average, yet small enough to avoid contributions from edge sites. We find that the extracted transition point remains approximately constant at $v_c \approx 0.7$ for all considered system sizes (right panel), showing a consistent behaviour of the normal to FQH states phase transition across the lattice-continuum crossover. The value $v_c > 0.5$ may be explained by edge effects, which are present at the phase transition even for large L because the transition occurs when there are just enough fluxes through the lattice to host a two-boson FQH state. Although it is challenging to evaluate this effect quantitatively, our calculations of orbital occupations (see section titled ‘Further numerical signatures of the FQH state’) show that the two bosons occupy three orbitals in the FQH regime, as expected from the few-particle expression $N_\phi = 2N - 1$.

Doublon suppression (Fig. 3): in the 3×3 system, we compute the doublon probability p_{Doublon} and find a sharp reduction at the transition point $\phi_c/2\pi$ (Extended Data Fig. 4b). We quantify the reduction by the suppression ratio $p_{\text{Doublon}}^{\text{FQH}}/p_{\text{Doublon}}^{\text{Normal}}$. The probability $p_{\text{Doublon}}^{\text{Normal}}$ ($p_{\text{Doublon}}^{\text{FQH}}$) is extracted from an interval of $\Delta\phi/2\pi = 0.02$ just before (after) the transition point. The resulting suppression ratio of about 3% is already remarkably close to the large-system limit of approximately 3% (right panel), suggesting an efficient screening of on-site interactions already in the 3×3 system.

Density correlations (Fig. 4): in Extended Data Fig. 4c, we show the reduced density correlations $g^{(2)}(|\mathbf{d}|)$. We find a depletion of correlations at $|\mathbf{d}|$ followed by an increase with the radial distance, which shows that the vortex structure is already present in the 3×3 system. As the system size is increased, the correlations at $|\mathbf{d}|$ approach zero, whereas at a distance of $|\mathbf{d}| = 3l_B$, they stabilize at a value between one and two (right panel).

Fractional Hall conductivity (Fig. 5): we obtain the bulk density from an average over all sites within a radial distance $|\mathbf{d}| = 3l_B$ from the central site. For the 3×3 system, this corresponds to all sites except for the corner sites; as L increases, this condition includes sites within a circle with a diameter of about half the length of the system. We extract the Hall conductivity from a fit over an interval of $\Delta\phi_c/2\pi = 0.1\phi_c/2\pi$ with Středa’s formula. The left panel of Extended Data Fig. 4d shows the density at flux $\phi/2\pi \approx 0.34$, approximately at the centre of the fitting

window. When increasing the system size, the extracted Hall conductivity rapidly converges towards the fractional value of $\sigma_H/\sigma_0 = 1/2$, in agreement with the expectation for the thermodynamic limit (right panel).

Further numerical signatures of the FQH state. We also verify the presence of a FQH state by computing its orbital occupations. The $v = 1/2$ Laughlin state with N bosons occupies $2N - 1$ orbitals in the lowest Landau level in the disc geometry. The distribution of the occupations approaches a uniform distribution in the thermodynamic limit; in finite systems, it shows moderate variations thereof.

We first study a system with $N = 4$ bosons on 7×7 lattice sites and repulsive interactions $U = 8J$ (Extended Data Fig. 5a). The many-body spectrum shows three local minima of the energy difference between the group state and the first excited state, which we interpret as finite-size signatures of phase transitions. The occupation of the single-particle orbitals shows a qualitatively different distribution each time a minimum is crossed (histograms). Within the range $0.2 < \phi/2\pi < 0.3$, it agrees with the expectation of a four-particle $v = 1/2$ Laughlin state.

An unambiguous identification of the FQH state can be obtained through the PES⁵⁰. We choose the bipartition $N_A = N_B = 2$ of the particle sector. The PES is the spectrum of $-\log \hat{\rho}_A$, in which $\hat{\rho}_A = \text{Tr}_B \hat{\rho}$ is the reduced density matrix obtained by tracing $\hat{\rho} = |\Psi_0\rangle\langle\Psi_0|$ over subsystem B. Laughlin quasi-holes show a degeneracy resulting from a generalized exclusion principle, which is 15-fold in the present case of two bosons in seven orbitals. Indeed, we find a gap above the lowest 15 states within the flux range $0.2 < \phi/2\pi < 0.3$, confirming the FQH nature of the ground state in this parameter range.

We now turn to the experimentally studied system with $N = 2$ bosons on 4×4 lattice sites and repulsive interactions $U = 8J$ (Extended Data Fig. 5b). We find a single minimum in the energy spectrum between the ground state and the first excited state, indicating a finite-size precursor of a phase transition. The transition is shown by a change in the orbital occupation (histograms): the occupations change abruptly at the transition point, indicating a change of the ground state from absent orbital momentum to one with an orbital population that is in agreement with the prediction for a $v = 1/2$ Laughlin wavefunction. For the $N = 2$ system, the PES cannot provide a topological signature of the fractional Chern insulator, because a bipartition results in the spectrum of the single-particle density matrix that cannot scrutinize topological order.

For further numerical signatures on FQH states with $N \geq 3$, we refer the reader to ref. 28.

Absence of other topological states. Few-boson FQH systems may generally exhibit other topological states as well as the $v = 1/2$ Laughlin state. Two factors that determine the presence and the properties of these states are the particle number and the interaction range. In two-boson systems, several states cannot exist, such as fractions with a numerator larger than 2, the $v = 1$ bosonic Pfaffian state or the $v = 2/3$ Jain state. Indeed, for two bosons in a geometry with edges, the Pfaffian and $2/3$ Jain states would be supported by a single lowest-Landau-level orbital, owing to their respective relationship between number of particles and number of flux quanta on the plane geometry: $N_\phi = N - 1$ for the Pfaffian state, $N_\phi = N \times 3/2 - 2$ for the $v = 2/3$ Jain state⁵¹. Both two-body wavefunctions would thus be identical and topologically trivial condensates living in a 1D Hilbert space. Other FQH states with a smaller fraction, such as the $v = 1/4$ Laughlin state, could—in principle—be stabilized in a two-boson system, but would be gapless because of the on-site range of interactions. Indeed, as the flux is increased beyond the regime in which a gapped $v = 1/2$ Laughlin state is observed, the creation of quasi-hole states becomes possible at zero interaction energy cost. For on-site interactions, these quasi-hole states are degenerate (quasi-degenerate if lattice effects are taken into account) with the $v = 1/2$ Laughlin state and remain degenerate at larger flux. The

$v = 1/4$ Laughlin state (as well as other higher-order Laughlin states) can become the ground state at higher flux, but it will be degenerate with the $v = 1/2$ Laughlin state and its quasi-hole states⁵². So, we would not expect a gapped $v = 1/4$ FQH state as the ground state in this system and the $v = 1/2$ Laughlin state remains the most dilute FQH state for which we would expect a many-body gap for on-site interactions. These considerations hold for $\phi/2\pi < 0.3$; at flux $\phi/2\pi > 0.3$, numerical studies have shown that lattice effects lead to a more complex picture^{24,26,53}.

Data availability

The data that support the findings of this study are available in the Dataverse repository at <https://doi.org/10.7910/DVN/2XDSA4>.

48. Zupancic, P. et al. Ultra-precise holographic beam shaping for microscopic quantum control. *Opt. Express* **24**, 13881–13893 (2016).
49. Islam, R. et al. Measuring entanglement entropy in a quantum many-body system. *Nature* **528**, 77–83 (2015).
50. Sterdyniak, A., Regnault, N. & Bernevig, B. A. Extracting excitations from model state entanglement. *Phys. Rev. Lett.* **106**, 100405 (2011).
51. Regnault, N. & Jolicoeur, T. Quantum Hall fractions for spinless bosons. *Phys. Rev. B Condens. Matter Mater. Phys.* **69**, 235309 (2004).
52. Haldane, F. D. Fractional quantization of the Hall effect: a hierarchy of incompressible quantum fluid states. *Phys. Rev. Lett.* **51**, 605–608 (1983).
53. Möller, G. & Cooper, N. R. Fractional Chern insulators in Harper-Hofstadter bands with higher Chern number. *Phys. Rev. Lett.* **115**, 126401 (2015).

Acknowledgements We acknowledge fruitful discussions with B. Bakkali-Hassani, I. Carusotto, N. Cooper, J. Dalibard, A. Eckardt, S. Girvin, M. Hafezi, J. Ho, M. Lebrat, F. Palm, N. Ünal, K. Viebahn and M. Zwierlein. We are supported by grants from the National Science Foundation, the Gordon and Betty Moore Foundation's EPiQS Initiative, an Air Force Office of Scientific Research MURI programme, an Army Research Office MURI programme, the Swiss National Science Foundation (J.L.) and the NSF Graduate Research Fellowship Program (S.K.). F.G. acknowledges funding by the DFG through Research Unit FOR 2414 (project number 277974659) and through EXC-2111 (project number 390814868), and from the ERC through the European Union's Horizon 2020 (grant agreement no 948141). N.G. acknowledges funding through the EOS project CHEQS, the FRS-FNRS and the ERC grants TopoCold and LATIS.

Author contributions J.L., S.K., J.K. and P.S. contributed to conducting the experiment, collecting and analysing the data and performing the numerical calculations. J.L. proposed the experiment and performed supporting theoretical studies together with F.G., C.R. and N.G. All authors contributed to writing the manuscript and to discussions. M.G. supervised the work.

Competing interests M.G. is cofounder and shareholder of QuEra Computing. All other authors declare no competing interests.

Additional information

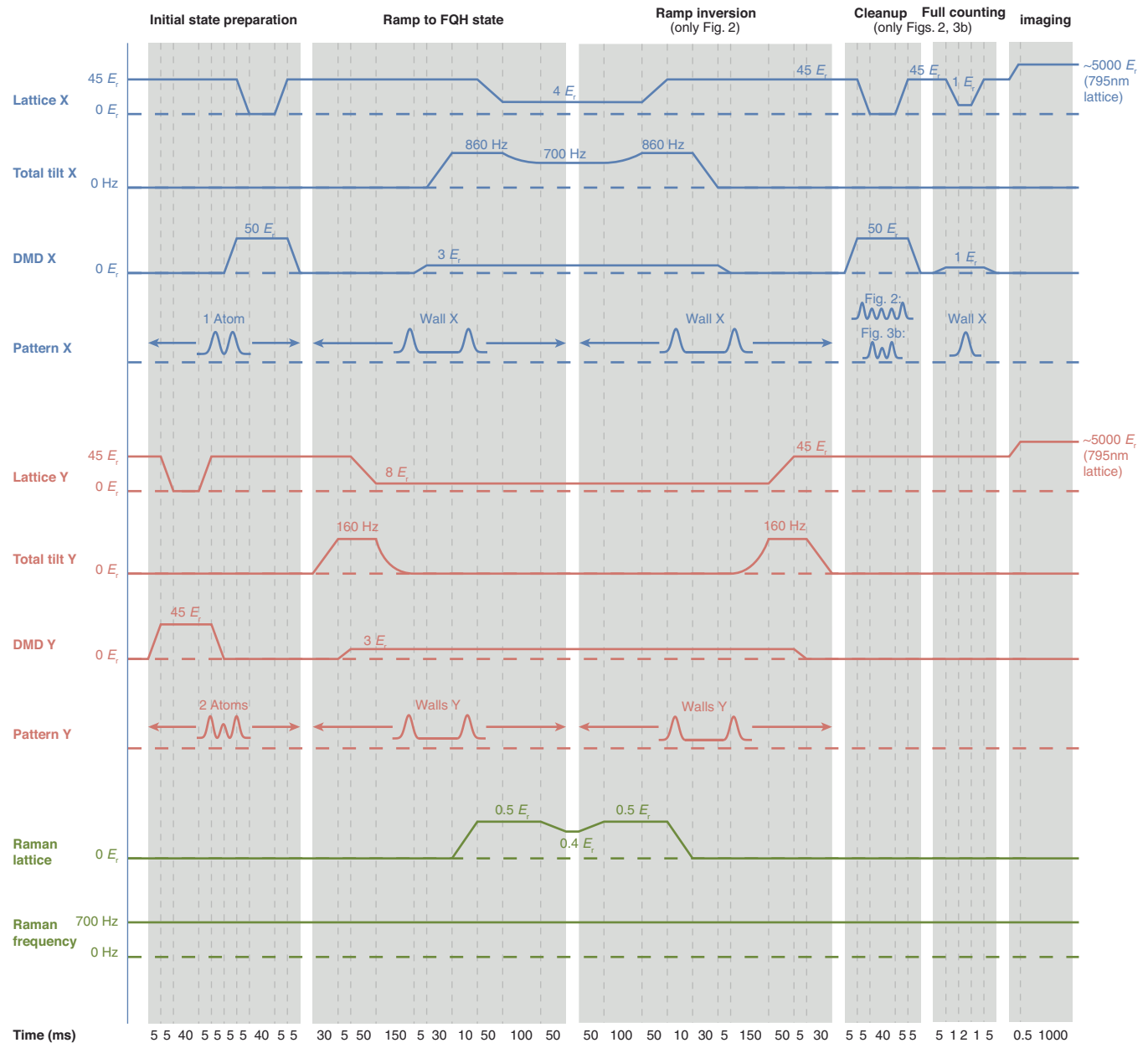
Supplementary information The online version contains supplementary material available at <https://doi.org/10.1038/s41586-023-06122-4>.

Correspondence and requests for materials should be addressed to Julian Léonard.

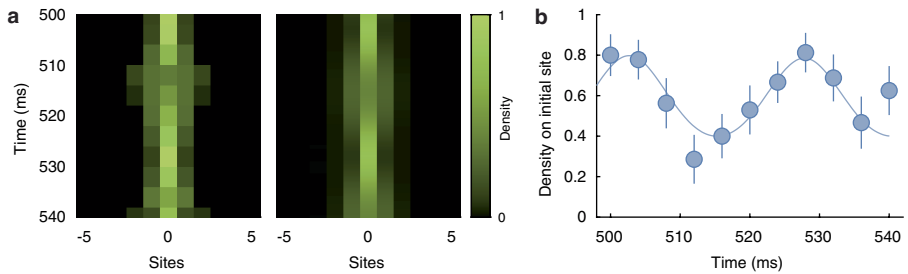
Peer review information *Nature* thanks David Feder and the other, anonymous, reviewer(s) for their contribution to the peer review of this work. Peer reviewer reports are available.

Reprints and permissions information is available at <http://www.nature.com/reprints>.

Article



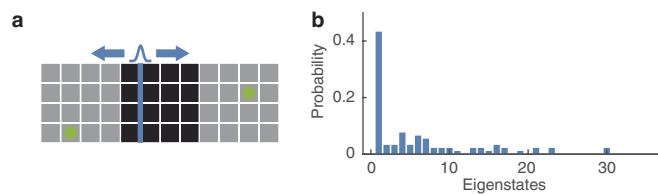
Extended Data Fig. 1 | Sequence. Full sequence for the performed experiments. All parameters are given for the driven Bose–Hubbard Hamiltonian (not the effective Hamiltonian).



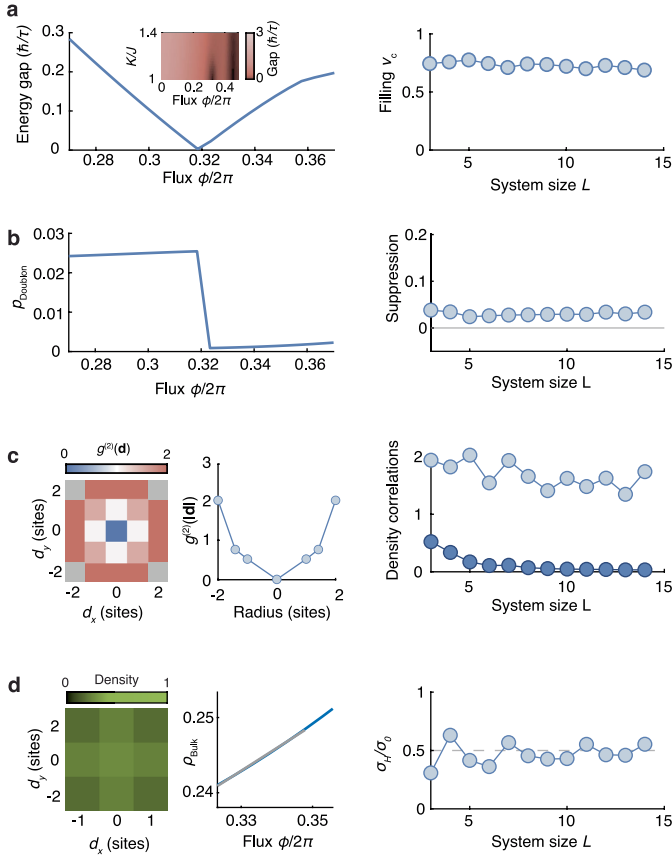
Extended Data Fig. 2 | Coherence time. **a**, Long-term evolution of an atom under 1D Raman tunnelling. The atom initially occupies site 0. The tunnelling along x is set to $K/2\pi = 13$ Hz (smaller than for the main measurements) and the tilt along x is $\Delta_x/2\pi = 40$ Hz per site. The tilt leads to a repassing of the quantum walk and converts it to Bloch oscillations, which show coherent revivals after

the evolution times of 500 ms. The evolution is in agreement with a fit to the data, which incorporates decoherence through the Monte Carlo wavefunction technique. **b**, Cut through the data in **a** of the initial site 0. The fit result (solid line) yields a decay rate of $\tau_{\text{Raman}} = 1.25(7)$ s. Error bars denote the s.e.m.

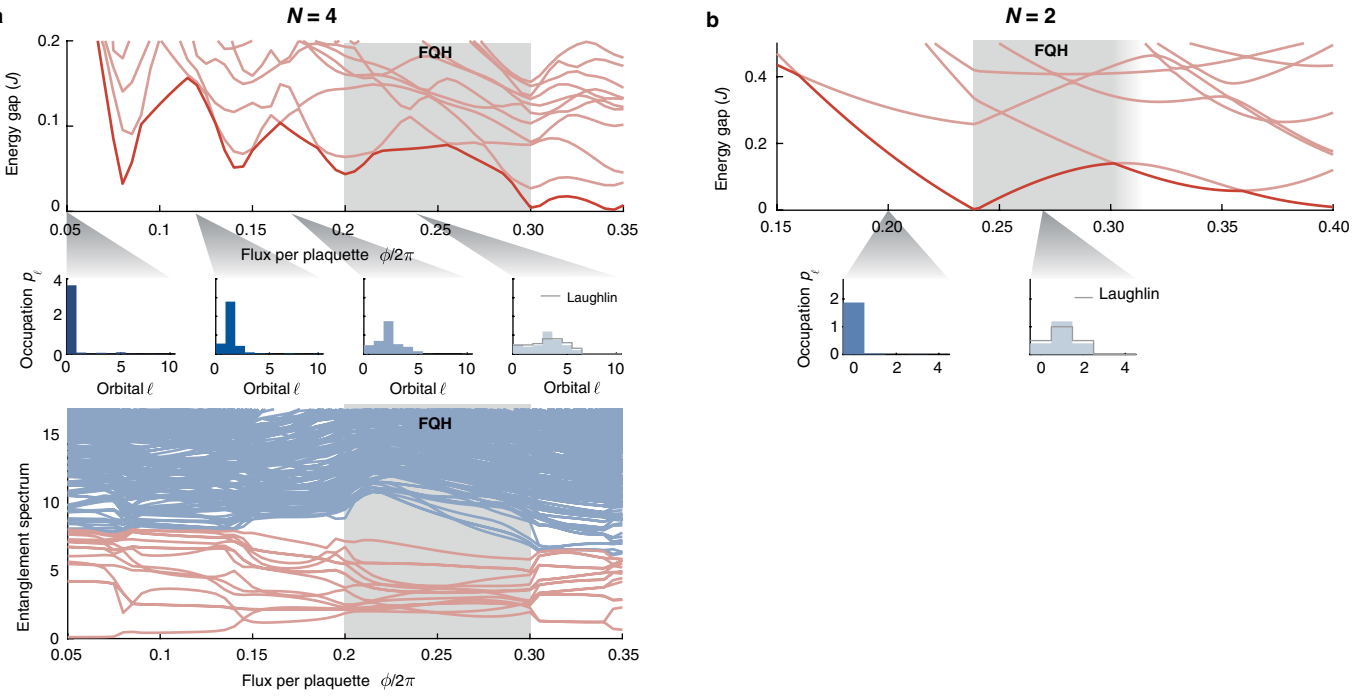
Article



Extended Data Fig. 3 | Excited-state populations. **a**, Protocol for measuring the full density distribution in the left two columns. We project a repulsive wall potential between the left two columns and enable tunnelling along the horizontal direction, thereby ejecting the atoms into half-rows and breaking up potential doublons. This allows us to identify the populations of the lowest 36 Fock states in energy. Fock states that are higher in energy involve at least one atom in the right two columns; their populations are allotted to their low-energy counterpart with both atoms in the left two columns. **b**, Excited-state populations. Inferred excited-state overlap $\langle \psi_i | \hat{\rho}_{\text{Final}} | \psi_i \rangle$ of the prepared state $\hat{\rho}_{\text{Final}}$ with the eigenstates $|\psi_i\rangle$ of the final Hamiltonian. We find a dominant population in the ground state and most of the excited-state population in the lowest few eigenstates.



Extended Data Fig. 4 | System-size scaling. Numerical system-size scaling of the observed FQH signatures for $N=2$ particles in quadratic box potentials. Left panels show data for a 3×3 system and right panels show the behaviour when increasing the length L of the system. **a**, Energy-gap diagram with a gap closing at the flux $\phi_c/2\pi$ for tunnelling $K/J=1$. For each system size, we compute the corresponding filling factor using $v_c=\rho_{\text{Bulk}}/(\phi_c/2\pi)$ (right panel). **b**, Doublon fraction with suppression at $\phi_c/2\pi$. We extract the ratio $p_{\text{Doublon}}^{\text{FQH}}/p_{\text{Doublon}}^{\text{Normal}}$ from the doublon fraction $p_{\text{Doublon}}^{\text{FQH}}$ in the FQH state and $p_{\text{Doublon}}^{\text{Normal}}$ in the normal state, each extracted over an interval of $\Delta\phi=0.1\times\phi_c$. **c**, The reduced density correlations show already the vortex pattern for the 3×3 system (left panel). As the system size is increased, the correlations for neighbouring sites ($|\mathbf{d}|=1$, dark blue) approach zero and the correlations at a distance of $3l_B$ (light blue, similar to Fig. 4c) stabilize at a value between one and two. **d**, Increase of the bulk density and extracted Hall conductivity σ_H/σ_0 from a linear fit by means of Středa's formula. When increasing the system size, the obtained Hall conductivity converges to $\sigma_H/\sigma_0=1/2$.



Extended Data Fig. 5 | Orbital occupations and topological properties for systems with $N = 2$ and $N = 4$ bosons. **a,** We first consider a system with $N = 4$, $U = 8$ /and 7×7 lattice sites. The many-body spectrum shows several local minima between the ground state and the first excited state (dark red), which we interpret as finite-size signatures of phase transitions. In the range $0.20 < \phi/2\pi < 0.3$, between two such minima, the occupations of the single-particle orbitals (histograms) approximately match the expectation for a Laughlin state. This interpretation is reinforced by the PES, which shows a gap

between the lowest 15 eigenstates (red) and all higher-lying states (blue), indicating (quasi-)degenerate quasi-hole states that identify the Laughlin state. **b,** For a system with $N = 2$, $U = 8$ /and 4×4 lattice sites, we find only a single local minimum between the ground state and the first excited state ($\phi/2\pi \approx 0.25$), which we interpret as the transition from the normal to FQH states. This is confirmed by the large overlap of the ground-state occupations of the single-particle orbitals with the Laughlin state. For the $N = 2$ system, an identification of the topological signatures in FQH states with the PES is not possible.